

The nature of the Roberge-Weiss transition in $N_f = 2$ QCD with Wilson fermions

Owe Philipsen* and Christopher Pinke†

Institut für Theoretische Physik - Johann Wolfgang Goethe-Universität, Germany

Max-von-Laue-Str. 1, 60438 Frankfurt am Main

(Dated: February 5, 2014)

At imaginary values of the quark chemical potential μ , Quantum Chromodynamics shows an interesting phase structure due to an exact center, or Roberge-Weiss (RW), symmetry. This can be used to constrain QCD at real μ , where the sign problem prevents Monte Carlo simulations of the lattice theory. In previous studies of this region with staggered fermions it was found that the RW endpoint, where the center transition changes from first-order to a crossover, depends non-trivially on the quark mass: for high and low masses, it is a triple point connecting to the deconfinement and chiral transitions, respectively, changing to a second-order endpoint for intermediate mass values. These parameter regions are separated by tricritical points. Here we present a confirmation of these findings using Wilson fermions on $N_\tau = 4$ lattices. In addition, our results provide a successful quantitative check for a heavy quark effective lattice theory at finite density.

PACS numbers: 12.38.Gc, 05.70.Fh, 11.15.Ha

Keywords: QCD phase diagram

I. INTRODUCTION

The QCD phase diagram at finite temperature T and chemical potential μ is currently under investigation both theoretically and experimentally, with a particular interest in the search for a potential critical endpoint (CEP). Because of its non-perturbative nature at the energy scales of interest, the only theoretical method to access QCD without truncations is via simulations of its discretized version, Lattice QCD (LQCD). At zero quark chemical potential μ , the nature of the thermal QCD transition for $N_f = 2 + 1$ flavors depends on the quark mass configuration. For degenerate infinitely heavy or massless quarks, there are first-order deconfinement and chiral phase transitions, respectively, at some critical temperatures T_c . In the vicinity of these limits, there are regions of first-order transitions which are separated by $Z(2)$ second-order lines from a crossover region, where the physical point is located [1, 2]. The nature of the transition in the $N_f = 2$ chiral limit is not settled yet. A recent review of the phase diagram from the lattice is provided in [3].

At finite real chemical potential, the fermion determinant becomes complex. This so-called sign problem prevents simulations using importance sampling. By contrast, at purely imaginary values of the chemical potential, $\mu = i\mu_i, \mu_i \in \mathbb{R}$, there is no sign problem and standard simulation techniques can be applied. In particular, the critical lines separating the first-order from the crossover regions continue as critical surfaces to imaginary chemical potential and terminate in tricritical lines at $\mu_i = \pi T/3$ [4, 5]. Their location constrains the phase diagram at zero and real μ and in particular explains the negative curvature of the chiral critical surface at $\mu = 0$

obtained previously [2, 6].

So far, LQCD studies at imaginary chemical potential have been carried out predominantly using the staggered fermion discretization, investigations with Wilson fermions have only been started recently [7–10]. An independent confirmation of the phase structure found in [4, 5] with a different discretization is of high interest because of potential problems with the rooting of staggered fermions [11]. Furthermore, a three-dimensional effective theory of LQCD based on the hopping expansion of Wilson fermions has been put forward recently, which allows to simulate heavy quarks at all chemical potentials [12]. The full LQCD results presented here provide a successful check of the predictive power of the effective theory.

II. THE ROBERGE-WEISS SYMMETRY

The grand canonical partition function of QCD for arbitrary quark masses and at finite chemical potential is even under charge conjugation. Moreover it is invariant under non-trivial global center transformations of the gauge group, provided the quark chemical potential is shifted by a center element. These exact symmetries read

$$Z(\mu) = Z(-\mu), \quad (1)$$

$$Z(\mu) = Z(\mu + 2\pi i k / N_c), \quad k \in \mathbb{N}. \quad (2)$$

The periodicity in the imaginary chemical potential is called Roberge-Weiss (RW) symmetry [13], for an elementary introduction see [14]. The general phase structure due to these symmetries was worked out in [13] and is shown in Figure 1. For the critical values

$$\mu_i^c = (2k + 1) \pi T / N_c, \quad k = 0, 1 \dots N_c - 1, \quad (3)$$

there are transitions between adjacent $Z(N_c)$ sectors of the theory. A particular center sector can be identified by

* philipsen@th.physik.uni-frankfurt.de

† pinke@th.physik.uni-frankfurt.de

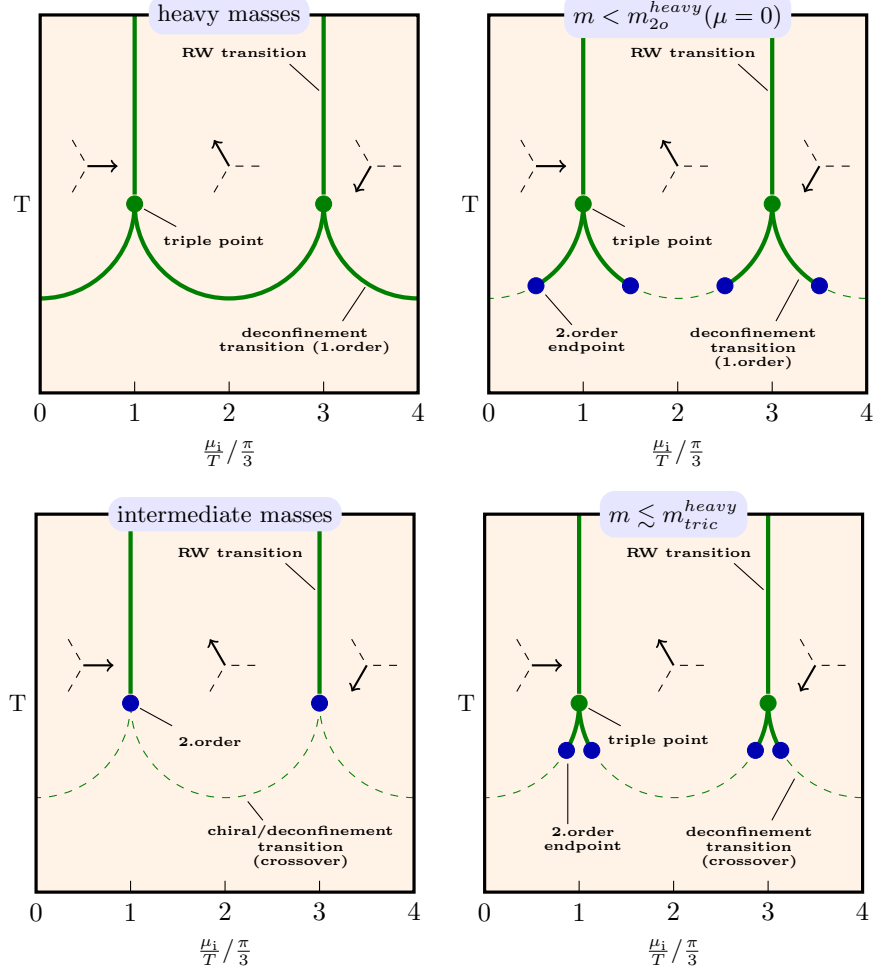


Figure 1. Schematic phase diagram of QCD at imaginary chemical potential. The solid vertical lines show the first-order RW-transitions at μ_i^c between the different $\mathbb{Z}(N_c)$ sectors, which are characterized by the phase of the Polyakov loop. Below T_c , the RW transitions are crossover. Beginning in the top left corner, the quark mass is decreased clockwise, changing the nature of the deconfinement and chiral phase transitions as indicated.

the phase of the Polyakov loop $L = |L|e^{i\phi}$. However, due to the periodicity of the partition function all physical observables are invariant under shifts $\mu_i + 2\pi k/N_c$. At low temperatures the transition between adjacent sectors is a crossover whereas it is a first-order phase transition at high temperatures [13, 15, 16]. Consequently, the first-order Roberge-Weiss transition has an endpoint. On the other hand, the deconfinement and chiral transition lines extend into the μ_i region and meet the first-order RW line in the RW endpoint [4, 5]. Therefore the nature of this end- or meeting point is non-trivial and depends on N_f and the fermion mass. This is sketched in Figure 1. For large masses, the deconfinement transition at $\mu = 0$ is of first-order and joins the RW endpoint, which is a triple point. As the mass is lowered, the $\mu = 0$ transition passes through the second-order line and becomes a crossover. This carries over to the μ_i region where the second-order point approaches the RW endpoint from $\mu = 0$ with decreasing mass. The remaining first-order

line shrinks until it eventually meets the RW point. At this mass value one has a tricritical point. The same happens when coming from the chiral limit, increasing the mass, at least for $N_f = 2, 3$ [4, 5]. For fixed flavor content and for $\mu_i = \mu_i^c$, there is then a phase diagram as in Figure 2, showing the nature of the RW endpoint as a function of quark mass. An order parameter can be defined by introducing the modified Polyakov loop $\hat{L} = Le^{i\theta} = |\hat{L}|e^{i\varphi}$. Its phase φ indicates the $\mathbb{Z}(N_c)$ sector the system is currently in and its average takes on the values zero and $k(2\pi/N_c)$, $k = 0, \dots, N_c - 1$, for the low and high temperature phases, respectively.

For $\mu_i < T\pi/N_c$, the chiral and deconfinement critical lines $m_c(\mu)$ emanate from the two tricritical points and continue to $\mu \geq 0$, thus constraining the physical phase diagram [4, 5]. Mapping the chiral critical line may also allow to clarify the nature of the transition in the $N_f = 2$ chiral limit, see e.g. [17].

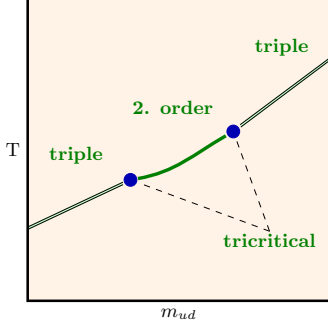


Figure 2. RW endpoint as function of mass (schematic).

III. LATTICE ACTION, OBSERVABLES AND SIMULATION PARAMETERS

For this study we employ the standard Wilson gauge action,

$$\mathcal{S}_{\text{gauge}} = \beta \sum_n \sum_{\mu, \nu > \mu} \{1 - \text{Re Tr}_c(P_{\mu\nu}(n))\} , \quad (4)$$

with plaquette $P_{\mu\nu}$ and lattice coupling $\beta = \frac{2N_c}{g^2}$, lattice sites n and Dirac indices μ, ν . We consider $N_f = 2$ mass-degenerate quarks with the standard Wilson action

$$\mathcal{S}_f[\bar{\psi}, \psi, U] = a^4 \sum_{N_f} \sum_{n, m} \bar{\psi}(n) D(n, m)[U] \psi(m) , \quad (5)$$

with fermion matrix

$$D(n, m) = \delta_{nm} - \kappa \sum_{i=1}^3 \left\{ (1 - \gamma_i) U_{\pm i}(n) \delta_{n+\hat{i}, m} \right\} \\ - \kappa \left\{ (1 - \gamma_0) e^{+a\mu} U_0(n) \delta_{m, n+\hat{0}} \right. \\ \left. + (1 + \gamma_0) e^{-a\mu} U_0^\dagger(m) \delta_{m, n-\hat{0}} \right\} . \quad (6)$$

Shorthand notation $\gamma_{-\mu} = -\gamma_\mu$ and $U_{-\mu}(n) = U_\mu^\dagger(n - \vec{\mu})$ has been used. In this formulation, the bare fermion mass m is encapsulated in the hopping parameter

$$\kappa = (2(am + 4))^{-1} . \quad (7)$$

Finite temperature on the lattice is given by

$$T = 1 / (a(\beta)N_\tau) . \quad (8)$$

As observables we use the order parameters for center and chiral symmetry breaking, respectively, i.e. the Polyakov loop at spatial site \mathbf{n}

$$L(\mathbf{n}) = \frac{1}{V} \text{Tr}_c \Pi_{x_0=0}^{N_\tau-1} U_0(x_0, \mathbf{n}) , \quad (9)$$

and the chiral condensate

$$\langle \bar{\psi} \psi \rangle = N_f \text{Tr} D^{-1} . \quad (10)$$

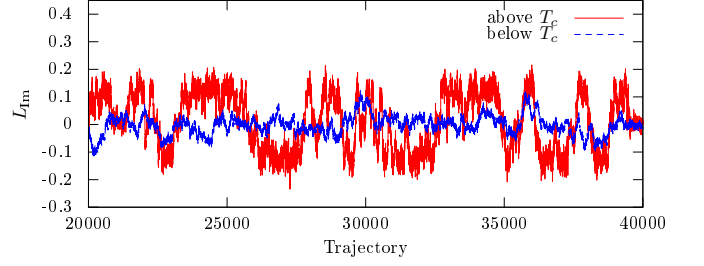


Figure 3. HMC history of L_{Im} at $\kappa = 0.1$ and $N_\sigma = 12$, above and below T_c

Non-analytic phase transitions only exist in the thermodynamic limit $V \rightarrow \infty$. To extract them from finite volume simulations, an extrapolation including a finite size scaling study must be employed. We use the Binder cumulant [18] constructed from $X = L_{\text{Im}}$,

$$B_4(X) = \langle (X - \langle X \rangle)^4 \rangle / \langle (X - \langle X \rangle)^2 \rangle^2 . \quad (11)$$

Its value in the thermodynamic limit for different orders of the phase transition is summarized in Table I. The leading finite-size corrections are given by a Taylor expansion (cf. [4])

$$B_4(\beta, N_\sigma) = B_4(\beta, \infty) + a_1(\beta - \beta_c) N_\sigma^{1/\nu} \\ + a_2((\beta - \beta_c) N_\sigma^{1/\nu})^2 + \dots . \quad (12)$$

Alternatively, the transition temperature may be extracted from the peak of the susceptibility

$$\chi(X) = V \langle (X - \langle X \rangle)^2 \rangle . \quad (13)$$

In the vicinity of the transition point, χ is expected to scale according (cf. [5]):

$$\chi = N_\sigma^{\gamma/\nu} f(t N_\sigma^{1/\nu}) . \quad (14)$$

Here, f is a universal scaling function, t is the reduced temperature $t = (T - T_c)/T_c$ and γ, ν are critical exponents specific to the universality class of the transition [19] (see Table I). With f unknown, the critical exponents can be estimated by looking at $\chi/N_\sigma^{\gamma/\nu}$ against $t N_\sigma^{1/\nu}$ for multiple spatial volumes. These curves should coincide for the correct values of ν and γ (collapse plot) and we use them to check the values for ν determined from the Binder cumulant.

All simulations presented below were carried out using the OpenCL [20] based code CL²QCD [21], which runs efficiently on Graphic Processing Units (GPUs) on LOEWE-CSC [22] at Goethe-University Frankfurt and on SANAM at GSI Darmstadt (see e.g. [23]). We work at fixed temporal lattice extent $N_\tau = 4$ and $\mu_i^c = \pi T$. In order to determine the phase diagram, Figure 2, we simulated 24 mass values ranging from $\kappa = 0.03 \dots 0.165$. For the finite size scaling, each κ was simulated on at least three, in some cases four or five spatial volumes, ranging from $N_\sigma = 8$ to 20. To scan the temperature, at least

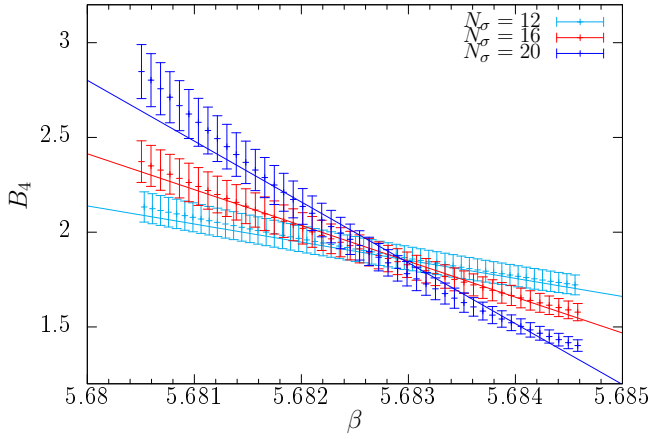


Figure 4. Reweighted Binder Cumulant of L_{Im} at $\kappa = 0.07$ for various N_σ , including the fits to the finite size scaling form.

ten β -values with $\Delta\beta = 0.001$ around T_c have been simulated on each lattice. In each run, 35k HMC trajectories of unit length have been produced after 5k trajectories of thermalization. In some cases this number has been extended to 75k. The acceptance rate in each run was of the order of 75%. Additional β -points have been filled in using Ferrenberg-Swendsen reweighting [24]. Details about the simulations can be found in Table III in the Appendix.

	Crossover	3D Ising	triple point	tricritical
$B_4(X)$	3	1.604	1.5	2
ν	-	0.6301(4)	1/3	1/2
γ	-	1.2372(5)	1	1

Table I. Values for the Binder cumulant $B_4(X)$ [4] and critical exponent ν for different phase transitions [25].

IV. NUMERICAL RESULTS

At fixed value of μ_i on the boundary between center sectors, the phase of the Polyakov loop, or its imaginary part L_{Im} , fluctuates between the values realized in each sector. At high temperatures these fluctuations are jumps between two distinct non-zero values, while for lower temperatures they are realized smoothly around zero, as shown in Figure 3. Note that in both cases one has $\langle L_{\text{Im}} \rangle = 0$ for sufficiently large statistics. For high temperatures (in the first-order case), the system will eventually take on one of the possible values in the thermodynamic limit, i.e. the symmetry will break spontaneously. In the following, we study the nature of the RW endpoint as a function of the fermion mass in analogy to the staggered study [4].

Figure 4 shows the functional behavior of the Binder cumulant B_4 for one particular quark mass as the spatial volume is increased. B_4 decreases with β and gets

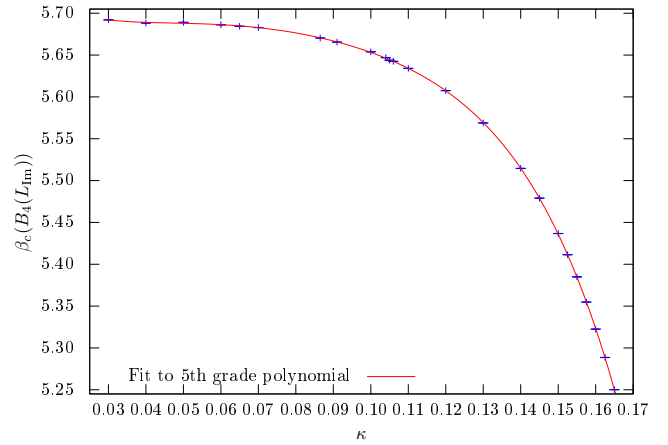


Figure 5. β_c as a function of κ , extracted from fits to B_4 data according to (12). Also shown is a fit to a fifth grade polynomial.

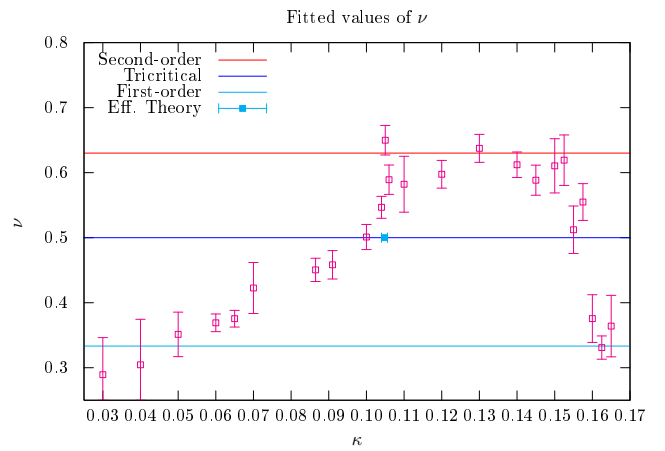


Figure 6. Fitted critical exponent ν as a function of κ . Also shown are values of ν for certain universality classes as well as the prediction for the tricritical mass from the effective theory [12].

steeper as the volume is increased. This is expected as below and above β_c a crossover and first-order region is located, which have a B_4 value of 3 and 1.5, respectively, in the thermodynamic limit, where B_4 approaches a step function. The intersection of the three finite volumes gives an estimate for the location of the RW endpoint. To extract it together with the critical exponent ν , we fit to the scaling form (12). The resulting value for $B_4(\beta, \infty)$ is found to be somewhat higher than the universal values because of large finite volume corrections, in agreement with the observations in staggered simulations [4]. The critical exponent ν , however, can be extracted quite well. This procedure is carried out for all simulated values of κ and the results for the critical coupling and exponent are collected in Figures 5 and 6, respectively.

Note how β_c shows a significant fermionic influence for $\kappa \gtrsim 0.085$ only, in accord with the nature of the phase

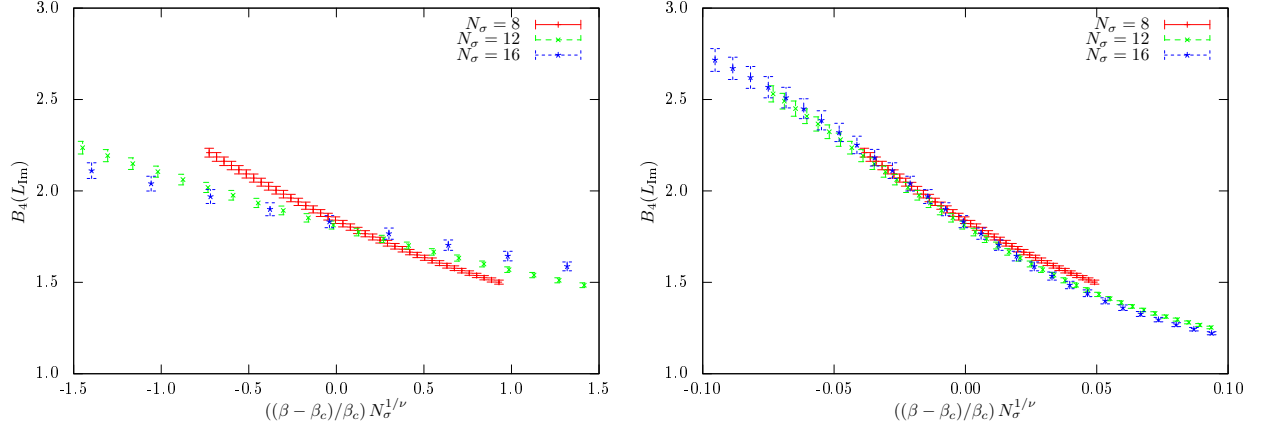


Figure 7. Collapse plots of $B_4(L_{\text{Im}})$ at $\kappa = 0.130$ for first- (left) and second-order (right) critical exponents.

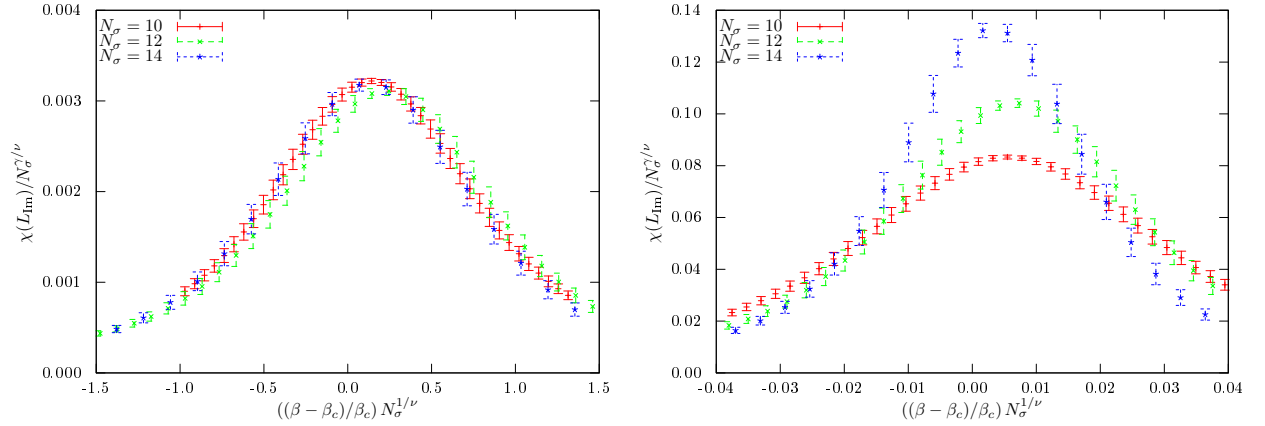


Figure 8. Collapse plots of $\chi(L_{\text{Im}})$ at $\kappa = 0.165$ for first- (left) and second-order (right) critical exponents.

transition, which stays first-order as in pure gauge theory in the large quark mass range. For intermediate masses, the RW endpoint is of second-order and changes back to triple point nature in the light mass region, where the RW transition meets with a first-order chiral transition.

The analysis of the Binder cumulant can be checked and confirmed by also looking at the susceptibilities of various observables. For $|L|$, L_{Im} and $\langle\bar{\psi}\psi\rangle$ fully consistent values for β_c are found from the peak of the susceptibility, see Tables IV, V and II in the Appendix.

The identification of the order of the transition can also be checked by collapse plots using the scaling form of B_4 as well as the susceptibilities. Figures 7 and 8 show examples for $\kappa = 0.130$ and 0.165 , respectively, allowing for a clear discrimination between different scaling scenarios, with $\kappa = 0.130$ in the second-order region and $\kappa = 0.165$ in the first-order region.

For lighter masses, the chiral transition is also seen in the melting of the chiral condensate $\langle\bar{\psi}\psi\rangle$ and the peak of its susceptibility, respectively. This is shown in Figure 9 (left), which shows $\langle\bar{\psi}\psi\rangle$ at $\kappa = 0.165$ for different N_σ . As the volume of the system is increased, the gradient

gets steeper, as expected to happen in a first-order transition. In addition, the collapse plot of $\chi(\langle\bar{\psi}\psi\rangle)$ in Figure 9 (right) clearly confirms first-order behavior. Our results in the small mass region partly support earlier ones from [9], where the authors simulated at various $\kappa \geq 0.155$ and find that these all lie in the first-order region. However, no analysis for a tricritical point has been carried out there.

Note that determining the order of the transition from collapse plots can be inconclusive if the exponents for different scenarios take on similar values, as is the case for second-order and tricritical exponents: $\gamma/\nu = 1.963$ and 2 , respectively. The identification of the tricritical points separating the triple point regions from second-order endpoint regions is thus best carried out using the Binder cumulant, cf. Figure 6.

We thus determine the two tricritical κ to be:

$$\kappa_{\text{heavy}}^{\text{tric}} = 0.1000 \pm 0.090, \quad (15)$$

$$\kappa_{\text{light}}^{\text{tric}} = 0.1550 \pm 0.050. \quad (16)$$

The errors on these values are chosen conservatively such that the neighboring simulation points which clearly fall

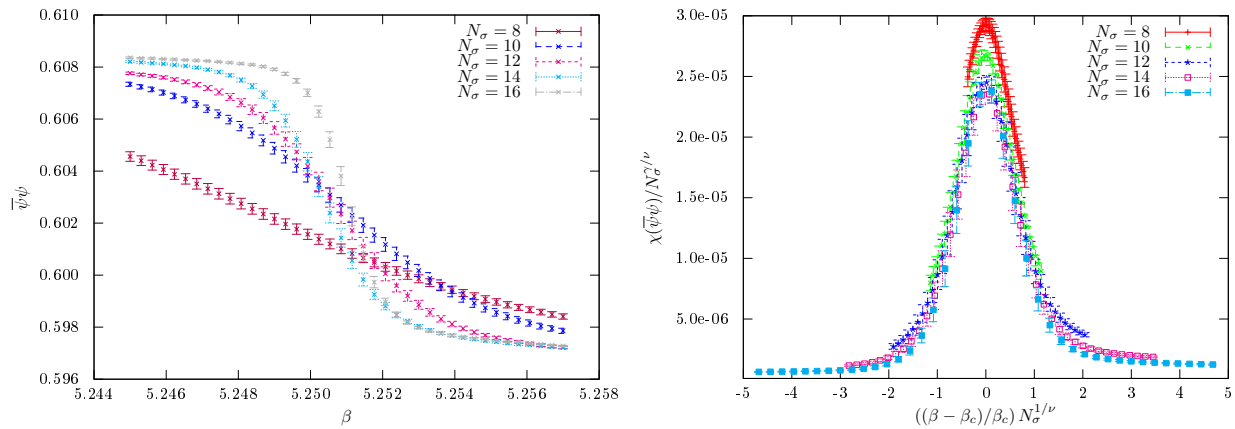


Figure 9. $\langle \bar{\psi}\psi \rangle$ at $\kappa = 0.165$ as N_σ is increased (left). Collapse plot of $\chi(\langle \bar{\psi}\psi \rangle)$ at $\kappa = 0.165$ according to first-order exponents (right).

into the first and second-order scenario, respectively, are taken as a boundary for the tricritical masses. In summary, the qualitative phase structure for the RW transition is exactly as for staggered fermions [4, 5].

Our results for the location of the tricritical points on $N_\tau = 4$ may also serve as a quantitative check for the predictions of an effective lattice theory for finite density [12], which includes the fermion determinant through order κ^2 only. There, the tricritical point in the heavy mass region was predicted to be

$$\kappa_{\text{heavy}}^{\text{tric}}(\text{eff. theory}) = 0.1048 \pm 0.0008, \quad (17)$$

in good agreement with the full LQCD simulations.

Finally, we estimate the pion mass m_π at the light tricritical point. To this end, $T, \mu = 0$ simulations at the tricritical couplings $\beta = 5.355, \kappa = 0.1575$ were run on a $16^3 \times 32$ lattice on JUQUEEN[26]. We generated 4200 trajectories after 500 trajectories of thermalization. On these, the effective masses for the pion and rho particle were estimated to be $am_\pi = 1.1426(17)$ and $am_\rho = 1.2147(25)$ [27]. Equating am_ρ to the physical value yields $m_\pi \approx 729(2)$ MeV and a lattice spacing of $a \approx 0.3$ fm. This corresponds to a ratio $m_\pi/m_\rho = 0.94064$, compared to the physical value of 0.18003, i.e. on coarse lattices the chiral first-order RW region is very wide.

V. SUMMARY AND PERSPECTIVES

We have performed a study of $N_f = 2$ QCD at imaginary value $\mu = i\pi T/3$ of the quark chemical potential, confirming an interesting phase structure seen earlier in simulations using staggered fermions. In particular, it was found that the endpoint of the transition between different center sectors is connected to the analytic continuation of the deconfinement and chiral transitions, and hence its nature depends non-trivially on the quark mass as in Figure 2. First-order regions at small and large quark masses are separated by two tricritical points from a second-order region at intermediate quark masses. In addition, we observe good agreement between the prediction of an effective lattice theory for the large mass tricritical point and our full simulation result. Cut-off effects on the location of the tricritical points are expected to be strong and can be studied by increasing N_τ , at significantly larger numerical cost. It might also be interesting to follow [17] and repeat the simulations at smaller values of imaginary chemical potential in order to determine the nature of the $\mu = 0$ transition in the chiral limit.

ACKNOWLEDGMENTS

O. P. and C. P. are supported by the Helmholtz International Center for FAIR within the LOEWE program of the State of Hesse. C.P. is supported by the GSI Helmholtzzentrum für Schwerionenforschung.

-
- [1] Y. Aoki, G. Endrodi, Z. Fodor, S. Katz, and K. Szabo, *Nature* **443**, 675 (2006), arXiv:hep-lat/0611014 [hep-lat].
 - [2] P. de Forcrand and O. Philipsen, *JHEP* **0701**, 077 (2007), arXiv:hep-lat/0607017 [hep-lat].

- [3] O. Philipsen, *Acta Phys.Polon.Supp.* **5**, 825 (2012), arXiv:1111.5370 [hep-ph].
- [4] P. de Forcrand and O. Philipsen, *Phys.Rev.Lett.* **105**, 152001 (2010), arXiv:1004.3144 [hep-lat].

- [5] C. Bonati, G. Cossu, M. D’Elia, and F. Sanfilippo, Phys.Rev. **D83**, 054505 (2011), arXiv:1011.4515 [hep-lat].
- [6] P. de Forcrand and O. Philipsen, JHEP **0811**, 012 (2008), arXiv:0808.1096 [hep-lat].
- [7] K. Nagata and A. Nakamura, Phys.Rev. **D83**, 114507 (2011), arXiv:1104.2142 [hep-lat].
- [8] K. Nagata and A. Nakamura, JHEP **1204**, 092 (2012), arXiv:1201.2765 [hep-lat].
- [9] L.-K. Wu and X.-F. Meng, Phys.Rev. **D87**, 094508 (2013), arXiv:1303.0336 [hep-lat].
- [10] A. Alexandru and A. Li, PoS **LATTICE2013**, 208 (2013), arXiv:1312.1201 [hep-lat].
- [11] S. R. Sharpe, PoS **LAT2006**, 022 (2006), arXiv:hep-lat/0610094 [hep-lat].
- [12] M. Fromm, J. Langelage, S. Lottini, and O. Philipsen, JHEP **1201**, 042 (2012), arXiv:1111.4953 [hep-lat].
- [13] A. Roberge and N. Weiss, Nucl.Phys. **B275**, 734 (1986).
- [14] O. Philipsen, (2010), arXiv:1009.4089 [hep-lat].
- [15] P. de Forcrand and O. Philipsen, Nucl.Phys. **B642**, 290 (2002), arXiv:hep-lat/0205016 [hep-lat].
- [16] M. D’Elia and M.-P. Lombardo, Phys.Rev. **D67**, 014505 (2003), arXiv:hep-lat/0209146 [hep-lat].
- [17] C. Bonati, M. D’Elia, P. de Forcrand, O. Philipsen, and F. Sanfilippo, (2013), arXiv:1311.0473 [hep-lat].
- [18] K. Binder, Z.Phys. **B43**, 119 (1981).
- [19] Strictly speaking, critical exponents can be defined for second-order transitions only. However, similar considerations can be carried out for the first-order case, too, cf. [28].
- [20] Khronos Working Group, “The OpenCL Specification,” [Http://www.khronos.org/registry/cl/](http://www.khronos.org/registry/cl/).
- [21] M. Bach, V. Lindenstruth, O. Philipsen, and C. Pinke, Comput.Phys.Commun. **184**, 2042 (2013), arXiv:1209.5942 [hep-lat].
- [22] M. Bach, M. Kretz, V. Lindenstruth, and D. Rohr, Computer Science - Research and Development , 1 (2011).
- [23] M. Bach, O. Philipsen, and C. Pinke, PoS **LAT2013** (2013).
- [24] A. M. Ferrenberg and R. H. Swendsen, Phys.Rev.Lett. **63**, 1195 (1989).
- [25] A. Pelissetto and E. Vicari, Phys.Rept. **368**, 549 (2002), arXiv:cond-mat/0012164 [cond-mat].
- [26] [Http://www.fz-juelich.de/ias/jsc/EN/Expertise/Supercomputers/JUQUEEN/JUQUEEN_node.html](http://www.fz-juelich.de/ias/jsc/EN/Expertise/Supercomputers/JUQUEEN/JUQUEEN_node.html).
- [27] We thank Georg Bergner for help with this analysis.
- [28] M. Fisher and A. Berker, Phys.Rev. **B26**, 2507 (1982).

Appendix: Simulation details

In this section, details about the results carried out in the setup described in Section IV will be given. An overview about the simulated systems can be seen in Table III. Analysis details are given in Tables V,II and IV. The results of the fits of the Binder cumulant to (12) are given in Table VI.

κ	β -range	$N_\sigma=8$	$N_\sigma=10$	$N_\sigma=12$	$N_\sigma=14$	$N_\sigma=16$	$N_\sigma=20$
0.1525	5.407-5.417	5.4120(6)	5.4132(3)	5.4128(2)	5.4128(2)	5.4126(1)	-
0.1550	5.380-5.389	-	5.3851(4)	-	5.3852(2)	-	-
0.1575	5.350-5.361	5.3552(5)	5.3553(3)	5.3554(2)	5.3555(1)	5.3553(1)	-
0.1600	5.319-5.330	5.3220(4)	5.3229(3)	5.3226(2)	5.3229(1)	5.3231(2)	-
0.1625	5.284-5.294	5.2867(4)	5.2875(2)	5.2879(2)	5.2881(1)	5.2882(2)	-
0.1650	5.246-5.256	5.2488(3)	5.2510(2)	5.2508(2)	5.2504(1)	5.2510(1)	-

Table II. Overview of β_c obtained from the peak of the susceptibility of $\langle \bar{\psi}\psi \rangle$.

κ	β -range	$N_\sigma=8$	$N_\sigma=10$	$N_\sigma=12$	$N_\sigma=14$	$N_\sigma=16$	$N_\sigma=20$
0.0300	5.685-5.696	-	40k	40k	40k	40k	-
0.0400	5.685-5.695	-	40k	40k	40k	40k	-
0.0500	5.683-5.695	-	40k	40k	40k	40k	-
0.0600	5.681-5.695	40k	40k	40k	40k	40k	(40k)
0.0650	5.676-5.689	40k	40k	80k	-	40k	-
0.0700	5.676-5.688	40k	-	40k	-	60k	80k
0.0865	5.662-5.678	40k	-	40k	-	60k	(80k)
0.0910	5.659-5.673	40k	-	40k	-	40k	80k
0.1000	5.647-5.658	40k	-	40k	-	40k	80k
0.1040	5.640-5.655	40k	-	40k	-	40k	-
0.1050	5.638-5.650	40k	-	40k	-	40k	-
0.1060	5.638-5.650	40k	-	40k	-	40k	-
0.1100	5.629-5.640	40k	-	40k	-	40k	80k
0.1200	5.602-5.613	40k	-	40k	-	40k	80k
0.1300	5.562-5.578	40k	-	40k	-	40k	-
0.1400	5.508-5.520	40k	-	40k	-	40k	-
0.1450	5.474-5.485	40k	-	40k	40k	40k	-
0.1500	5.431-5.441	40k	-	40k	-	40k	80k
0.1525	5.407-5.417	40k	40k	40k	40k	40k	-
0.1550	5.380-5.389	40k	40k	40k	40k	40k	-
0.1575	5.350-5.361	40k	40k	40k	40k	40k	-
0.1600	5.319-5.330	40k	40k	40k	40k	40k	-
0.1625	5.284-5.294	40k	40k	40k	40k	40k	-
0.1650	5.246-5.256	40k	40k	40k	40k	40k	-

Table III. Overview of simulations carried out at $\mu_i = i\pi T$ and $N_\tau = 4$. The numbers given denote the statistics produced on each β point. A given β -range was scanned with $\Delta\beta = 0.001$ for each N_σ . Numbers in brackets indicate that some β values have smaller statistics.

κ	β -range	$N_\sigma=8$	$N_\sigma=10$	$N_\sigma=12$	$N_\sigma=14$	$N_\sigma=16$	$N_\sigma=20$
0.0300	5.685-5.696	-	5.6903(6)	5.6905(4)	5.6906(3)	5.6915(2)	-
0.0400	5.685-5.695	-	5.6903(4)	5.6910(4)	5.6906(3)	5.6904(2)	-
0.0500	5.683-5.695	-	5.6892(4)	5.6898(3)	5.6904(3)	5.6897(2)	-
0.0600	5.681-5.695	5.6878(4)	5.6873(5)	5.6883(4)	5.6881(3)	5.6873(2)	-
0.0650	5.676-5.689	5.6869(6)	5.6857(4)	5.6856(2)	-	5.6855(2)	-
0.0700	5.676-5.688	5.6856(5)	-	5.6844(4)	-	5.6833(2)	5.6832(2)
0.0865	5.662-5.678	5.6745(5)	-	5.6723(3)	-	5.6714(2)	5.6716(1)
0.0910	5.659-5.673	5.6705(5)	-	5.6673(4)	-	5.6668(2)	5.6666(2)
0.1000	5.647-5.658	5.6565(6)	-	5.6550(3)	-	5.6545(3)	5.6547(1)
0.1040	5.640-5.655	5.6498(6)	-	5.6489(3)	-	5.6481(3)	-
0.1050	5.638-5.650	5.6488(5)	-	5.6469(3)	-	5.6460(3)	-
0.1060	5.638-5.650	5.6471(5)	-	5.6448(3)	-	5.6444(3)	-
0.1100	5.629-5.640	5.6385(6)	-	5.6365(4)	-	5.6360(3)	5.6360(2)
0.1200	5.602-5.613	5.6113(5)	-	5.6104(3)	-	5.6093(2)	5.6092(2)
0.1300	5.562-5.578	5.5743(5)	-	5.5725(2)	-	5.5715(2)	-
0.1400	5.508-5.520	5.5193(4)	-	5.5182(3)	-	5.5166(3)	-
0.1450	5.474-5.485	5.4828(4)	-	5.4817(3)	5.4812(2)	5.4807(2)	-
0.1500	5.431-5.441	5.4384(4)	-	5.4377(3)	-	5.4376(2)	5.4373(1)
0.1525	5.407-5.417	5.4137(3)	5.4131(3)	5.4129(2)	5.4127(2)	5.4124(2)	-
0.1550	5.380-5.389	5.3854(3)	5.3852(3)	5.3855(3)	5.3852(2)	5.3851(1)	-
0.1575	5.350-5.361	5.3560(3)	5.3555(3)	5.3555(2)	5.3555(1)	5.3554(2)	-
0.1600	5.319-5.330	5.3230(3)	5.3237(2)	5.3227(2)	5.3229(1)	5.3231(1)	-
0.1625	5.284-5.294	5.2876(3)	5.2877(2)	5.2880(2)	5.2881(1)	5.2880(1)	-
0.1650	5.246-5.256	5.2493(3)	5.2510(2)	5.2509(2)	5.2504(1)	5.2510(1)	-

Table IV. Overview of β_c obtained from the peak of the susceptibility of $|L|$.

κ	β -range	$N_\sigma=8$	$N_\sigma=10$	$N_\sigma=12$	$N_\sigma=14$	$N_\sigma=16$	$N_\sigma=20$
0.0300	5.685-5.696	-	-	-	-	-	-
0.0400	5.685-5.695	-	-	-	-	5.6920(4)	-
0.0500	5.683-5.695	-	-	-	5.6928(6)	5.6914(5)	-
0.0600	5.681-5.695	-	-	5.6897(5)	5.6888(3)	5.6873(3)	-
0.0650	5.676-5.689	-	-	5.6862(3)	-	5.6854(2)	-
0.0700	5.676-5.688	-	-	5.6847(4)	-	5.6832(2)	5.6831(2)
0.0865	5.662-5.678	5.6765(7)	-	5.6720(3)	-	5.6712(2)	5.6715(1)
0.0910	5.659-5.673	5.6707(6)	-	5.6671(4)	-	5.6666(2)	5.6665(2)
0.1000	5.647-5.658	5.6561(6)	-	5.6546(3)	-	5.6541(3)	5.6543(2)
0.1040	5.640-5.655	5.6493(6)	-	5.6484(3)	-	5.6476(2)	-
0.1050	5.638-5.650	5.6483(5)	-	5.6464(3)	-	5.6455(2)	-
0.1060	5.638-5.650	5.6465(5)	-	5.6442(3)	-	5.6439(3)	-
0.1100	5.629-5.640	5.6378(6)	-	5.6358(4)	-	5.6354(3)	5.6354(2)
0.1200	5.602-5.613	5.6106(5)	-	5.6094(3)	-	5.6085(3)	5.6085(2)
0.1300	5.562-5.578	5.5734(5)	-	5.5713(2)	-	5.5706(2)	-
0.1400	5.508-5.520	5.5181(4)	-	5.5169(3)	-	5.5155(3)	-
0.1450	5.474-5.485	5.4815(4)	-	5.4806(3)	5.4803(2)	5.4799(2)	-
0.1500	5.431-5.441	5.4372(4)	-	5.4367(2)	-	5.4369(1)	5.4368(1)
0.1525	5.407-5.417	5.4127(3)	5.4122(3)	5.4121(2)	5.4120(2)	5.4118(2)	-
0.1550	5.380-5.389	5.3845(3)	5.3844(3)	5.3848(3)	5.3847(2)	5.3847(1)	-
0.1575	5.350-5.361	5.3553(3)	5.3549(3)	5.3550(2)	5.3551(2)	5.3551(2)	-
0.1600	5.319-5.330	5.3224(3)	5.3232(3)	5.3224(2)	5.3226(1)	5.3229(2)	-
0.1625	5.284-5.294	5.2872(3)	5.2874(2)	5.2878(2)	5.2880(1)	5.2879(1)	-
0.1650	5.246-5.256	5.2490(3)	5.2509(2)	5.2508(2)	5.2504(1)	5.2510(1)	-

Table V. Overview of β_c obtained from the peak of the susceptibility of $|L_{\text{Im}}|$.

κ	N_σ	β_c	ν	$B_4(\beta, \infty)$	a_1	a_2	χ^2
0.0300	12,14,16	5.6921(3)	0.289(57)	2.37(4)	-0.016(29)	-	0.968
0.0400	12,14,16	5.6883(2)	0.305(70)	2.63(4)	-0.036(73)	-	0.983
0.0500	10,12,14,16	5.6891(1)	0.351(34)	2.18(2)	-0.089(66)	-	0.965
0.0600	10,12,14,16	5.6862(1)	0.369(14)	2.04(1)	-0.126(50)	0.005(3)	0.773
0.0650	10,12,16	5.6844(1)	0.375(13)	1.92(1)	-0.13(30)	0.007(3)	1.408
0.0700	12,16,20	5.6829(1)	0.423(39)	1.86(2)	-0.28(18)	-	1.029
0.0865	8,12,16	5.6704(1)	0.450(18)	1.89(1)	-0.378(09)	-	1.026
0.0910	8,12,16,20	5.6655(1)	0.458(22)	1.85(1)	-0.38(11)	0.062(34)	1.173
0.1000	8,12,16,20	5.6539(1)	0.501(19)	1.74(1)	-0.56(12)	-	0.952
0.1040	8,12,16	5.6469(1)	0.547(17)	1.77(1)	-0.79(11)	-	0.991
0.1050	8,12,16	5.6438(1)	0.650(23)	1.85(1)	-1.52(21)	-	1.019
0.1060	8,12,16	5.6425(1)	0.589(23)	1.82(1)	-1.10(18)	-	1.015
0.1100	8,12,16, 20	5.6341(1)	0.582(43)	1.80(1)	-1.08(38)	-	1.064
0.1200	12,16,20	5.6075(1)	0.598(21)	1.75(1)	-1.167(20)	0.40(14)	0.996
0.1300	8, 12, 16	5.5689(1)	0.637(22)	1.83(1)	-1.64(22)	-	0.860
0.1400	8, 12, 16	5.5146(1)	0.612(20)	1.83(1)	-1.59(21)	-	0.821
0.1450	8, 12, 16	5.4790(1)	0.588(23)	1.80(1)	-1.50(26)	-	1.003
0.1500	12, 16, 20	5.4367(1)	0.611(42)	1.66(2)	-2.12(69)	-	0.950
0.1525	10, 12, 14, 16	5.4114(1)	0.620(39)	1.76(2)	-2.51(66)	-	1.029
0.1550	10, 12, 14, 16	5.3849(1)	0.512(37)	1.67(1)	-1.26(46)	-	0.984
0.1575	12, 14, 16	5.3548(1)	0.555(28)	1.80(2)	-2.42(60)	2.15(1.05)	1.015
0.1600	8, 10, 12	5.3225(1)	0.376(37)	1.77(2)	-0.43(26)	-	0.997
0.1625	10, 12, 14	5.2886(1)	0.331(18)	1.58(1)	-0.16(07)	0.015(12)	0.983
0.1650	10, 12, 14	5.2501(1)	0.364(47)	2.15(6)	-0.67(61)	0.11(20)	0.981

Table VI. Overview of fits to $B_4(L_{\text{Im}})$ according to (12). The N_σ column indicates which datasets have been used in the fit, see also Table III. If no value for a_2 is given, the fit has been performed with the linear ansatz.